DEVELOPMENT AND VALIDATION OF A HIGH-VACUUM THERMAL CONDUCTIVITY TESTBED FOR AEROSPACE INTERFACE MATERIALS

Amy Chang
National Aeronautics and Space Administration (NASA) Marshall Space Flight Center,
Huntsville, Alabama 35808, USA

Deborah Hernandez
Amentum Space Exploration Division, Engineering Services and Science Capability
Augmentation (ESSCA) Contract, Huntsville, Alabama 35808, USA

ABSTRACT

Spacecraft thermal margins depend on the temperature penalty of installed interfaces, yet catalog conductivity omits bondline thickness, mating surfaces, preload, and environment. The Testbed for Advanced Interface Materials in Vacuum (TAIMV) addresses this engineering-data gap by converting ambient/vacuum temperature fields from a four-coupon stack into quantities usable in spacecraft thermal models. Its 17-node steady-state model resolves axial conduction, parasitic fixture paths, grease-filled contact, radiation, and ambient convection. Four monolithic checks gave axial heat-rate ratios of 0.90–1.02, and Braycote calibration self-recovery gave 2.20% casewise mean absolute percentage error (MAPE) and 2.85% maximum difference. With transferable fixture terms frozen, Krytox LVP tested cross-material transfer against a manufacturer-derived external relation. The six Krytox cases gave 2.28% MAPE, 5.10% maximum difference, and full-field residual root-mean-square values of 0.553 °C ambient and 1.306 °C vacuum. Installed-joint resistance spanned 6.39–7.15 × 10^{-4} m²·K/W for Braycote and 4.09–4.49 × 10^{-4} m²·K/W for Krytox, corresponding to 2.33–6.66 K per modeled interface over the tested heat-flux range. TAIMV therefore supplies directly usable installed-joint resistance and conductance, plus apparent installed conductivity and explicitly model-conditioned grease-conductivity/contact terms.

NOMENCLATURE, ACRONYMS, AND ABBREVIATIONS

Symbol	Definition
BLT	Bondline thickness
CMY	Cooper-Mikic-Yovanovich contact model
G	Thermal conductance [W/K]
k_{app}	Apparent installed conductivity [W/(m·K)]
k_{cond}	Grease conductivity [W/(m·K)]
k_{ref}	Comparator conductivity at the mean bondline temperature [W/(m·K)]
L	Applied bondline thickness [m]
MLI	Multilayer insulation
p	Nominal interface pressure [Pa]
Q	Heat-transfer rate [W]
R''	Areal thermal resistance [m²·K/W]

$R''_{contact}$	Modeled contact resistance [m²·K/W]
R''_{CMY}	Modeled grease-filled CMY contact resistance [m²·K/W]
$R''_{\mathrm{installation}}$	Fitted residual resistance [m²·K/W]
$h_{\mathrm{a}}, h_{\mathrm{g}}, h_{\mathrm{joint}}$	Asperity, grease-gap, and installed-joint conductance [W/(m²·K)]
σ_{eff}	Combined RMS roughness [m]
m_{eff}	Effective asperity slope [rad]
Φ^{-1}	Inverse standard normal distribution function
σ_{SB}	Stefan-Boltzmann constant [W/(m²·K⁴)]
u	Uncertainty [%]
RMS	Root mean square
RTD	Resistance temperature detector
SRSS	Root-sum-square sensitivity indicator [%]
TAIMV	Testbed for Advanced Interface Materials in Vacuum
TC	Thermocouple
TIM	Thermal interface material
Y	CMY mean-plane separation [m]
ΔT	Temperature difference [K or °C]

INTRODUCTION

Spacecraft thermal-control architectures often place several mechanical interfaces between a heat source and the ultimate radiator. In vacuum, installed-joint resistance can shift component temperatures, allowable dissipation, heater demand, and thermal margin.[1] The relevant engineering input is therefore the response of a specific thermal interface material (TIM), bond line thickness (BLT), surface roughness, preload, and fixture, not catalog bulk conductivity alone. This matters because spacecraft programs often must make thermal-margin decisions before a full preload, BLT, and repeatability campaign can be completed.

Flight-like evidence confirms this systems view. Steinfeld and Martins showed that data from small, uniformly compressed specimens do not necessarily transfer to perimeter-bolted electronics boxes with bowing, gaps, and nonuniform pressure.[2] Increased dissipation in the Hubble Space Telescope Science Instrument Control and Data Handler-2 similarly required a copper thermal link and interstitial material to recover thermal margin.[3] Fixture studies and TIM reviews identify separation, pressure, BLT, wetting, rheology, and aging as coupled determinants of installed performance.[4–6]

ASTM C1044-24 provides the guarded single-sided heat-flow framework relevant to the monolithic diagnostic.[7] ASTM D5470 is the closest standardized physical-test analogue because it separates bulk conductivity and contact resistance through steady-state thermal impedance measured across multiple thicknesses.[8] Broader measurement and simulation-oriented characterization literature also emphasizes fixture, bondline, and contact separation.[9,10] Unlike D5470, TAIMV evaluates a vacuum-capable installed interface at one applied thickness by combining monolithic axial consistency, casewise extraction, independent external-comparator transfer, full-field residuals, and sensitivity/contact ablation.

The central engineering question is whether a sparse fixture temperature field can support a useful installed-joint input without turning close model/comparator agreement into an unjustified claim of unique intrinsic conductivity. This conference paper tests three apparatus-level propositions: the monolithic coupon is consistent with a predominantly axial path; a Braycote-calibrated fixture transfers to Krytox with the external comparator withheld and transferable terms frozen; and the installed joint can be reported as resistance or conductance with an explicit uncertainty boundary. Evidence is reported with continuous diagnostics rather than retrospective binary thresholds.

National Aeronautics and Space Administration (NASA) technology-readiness guidance emphasizes evidence obtained in progressively relevant environments.[11] TAIMV addresses that need with an interchangeable ambient/vacuum fixture, common instrumentation, and explicit parasitic-path modeling. TAIMV's novelty is not another bulk-conductivity value; it is an evidence-separated extraction architecture that distinguishes axial consistency, calibration self-recovery, transfer to a different material, and the directly observed installed response. This matters to reviewers and spacecraft thermal modelers because each reported quantity is linked to the evidence that supports it. The paper follows that chain from apparatus design and axial consistency through Braycote self-recovery, independent Krytox transfer, direct joint output, and the final uncertainty boundary.

Apparent installed conductivity is the installed stack-equivalent value for the tested nominal bondline thickness and total joint resistance; it is the direct assembled-interface input. Grease conductivity is the model estimate after fixture, boundary, thickness, and contact terms are de-embedded. Its numerical value remains conditional on those assumptions and is not a traceable product certification. Model-conditioned contact resistance is the area-normalized non-bulk resistance assigned by the model. The apparent-installed-conductivity and contact-resistance relations are stated in Equations (1) and (2).

Equation (1) defines apparent installed conductivity,

$$k_{\text{app}} = \frac{L}{R''_{\text{joint}}}, \tag{1}$$

where k_{app} is apparent installed conductivity in W/(m·K), L is applied bondline thickness in m, and R''_{joint} is total area-normalized installed-joint resistance in m²·K/W.

Equation (2) defines model-conditioned contact resistance,

$$R''_{\text{contact}} = R''_{\text{CMY}} + R''_{\text{installation}}, \tag{2}$$

where $R''_{contact}$ is total area-normalized contact resistance, R''_{CMY} is physical grease-filled Cooper-Mikic-Yovanovich (CMY) resistance, and $R''_{installation}$ is the separate installation residual, all in m²·K/W.

METHODS

TAIMV uses a vertical, nominal 3 × 3 in (76.2 × 76.2 mm) heat-flow path. The production specimen comprises four 0.125 ± 0.002 in (3.175 ± 0.051 mm) Type 304 stainless-steel (SS304) coupons separated by three evaluated internal TIM bond lines. Repeating the joint amplifies a weak interface temperature signature; conversion to a per-interface quantity assumes that the three internal joints are equivalent and does not imply a typical flight layer count. A separate 0.500 ±

0.002 in (12.70 ± 0.05 mm) monolithic SS304 coupon supplies an axial energy-consistency diagnostic and is not used to calibrate internal joint resistance.

The fixture conditions the axial path with independently powered main and guard heaters, alloy 110 copper (Cu110) spreading/sensing plates, a G10 glass-epoxy isolator, and a temperature-controlled cold plate. The chamber, fixture, sensor layout, and multilayer-insulation (MLI) envelope are unchanged between ambient and vacuum operation. Four resistance temperature detectors (RTDs) and five Type-T thermocouples (TCs) resolve the axial field and monitor guard, cold-side, MLI, and chamber conditions; radiation, convection, guard coupling, and fixture conduction remain separate model branches in Figure 1. Fixture weight supplies the present nominal 3.10–3.60 kPa internal pressure.

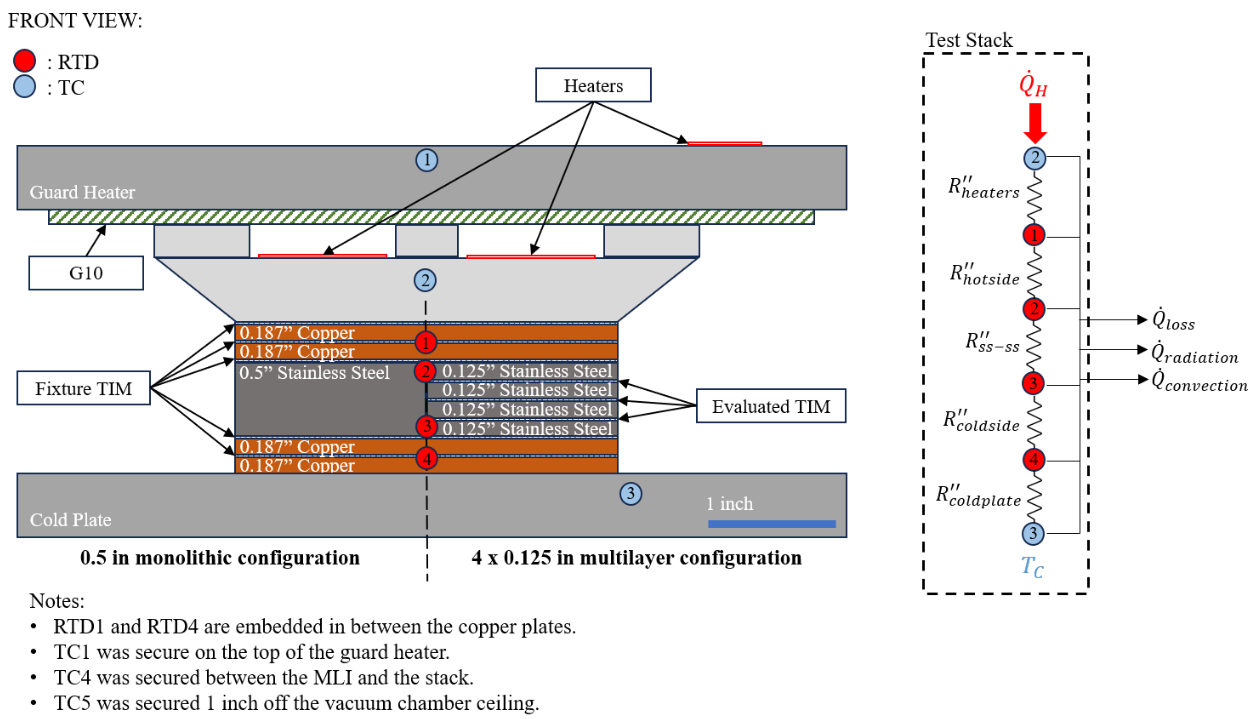

Figure 1. TAIMV stack and reduced heat path for the monolithic axial check and four-coupon, three-joint multilayer test configuration. Heights are not to scale.

Testing used a 12-in (305-mm) cube modular chamber from Ideal Vacuum and a Pfeiffer HiCube 80 turbomolecular station; the pump remained off for ambient operation. Vacuum-row inclusion used an operational limit of 1×10^{-4} Torr, with 1×10^{-5} Torr preferred. Braycote Cases B–D recorded 6×10^{-5} to 8×10^{-5} Torr, and Krytox Cases B–D recorded 1×10^{-5} Torr. Pressure is an operating-condition field, not traceable vacuum metrology or proof that residual-gas conduction is zero.

Cu110 sensing plates, each 0.187 ± 0.007 in (4.75 ± 0.18 mm) thick, are installed above and below the SS304 coupon region to promote lateral uniformity near the embedded RTDs. Zygo NewView 6000 optical-profiler measurements supplied root-mean-square roughness inputs of 1.60 µm for stainless-steel mating faces and 0.285 µm for copper mating faces.

The lower boundary is imposed with a Polystat CR250 temperature-controlled cold plate. Minco flexible resistance heaters provide main and guard heat input and are powered by an Extech Instruments 382270 quad-output direct-current supply. The guard heater and G10 isolator above the main heater reduce upward loss but remain a separately powered control volume. Two seven-layer MLI pieces wrap the top and sides of the test article, including the guard region, to reduce radiative exchange with the chamber.

Temperature instrumentation comprises five 30 American Wire Gauge Type-T thermocouples and four three-wire Class A Omega RTD-2-F3105-36-T-ROHS sensors. Thermocouples and RTD2–RTD3 are taped in place; RTD1 and RTD4 are epoxied into center grooves in the upper and lower copper sensing plates. A National Instruments data-acquisition system uses NI 9213 thermocouple and NI 9226 RTD modules.

RTD1 and RTD4 measure the upper and lower copper sensing plates; RTD2 and RTD3 monitor the SS304 region. In the monolithic coupon, their axial locations are 0.125 in (3.175 mm) and 0.370 in (9.398 mm) from the coupon top, giving a 0.245 in (6.223 mm) integration interval. TC1 measures the guard plate, TC2 the heater-side block, TC3 the cold plate, TC4 the local environment inside the MLI envelope, and TC5 the chamber environment. Figure 2 shows the chamber before MLI placement and the installed MLI configuration.

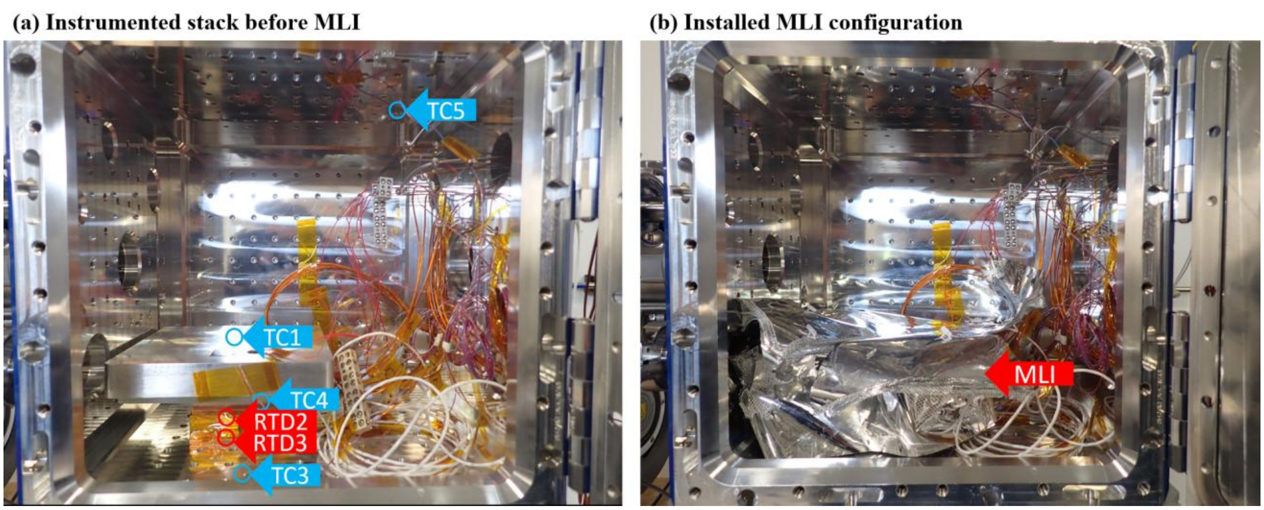

Figure 2. TAIMV inside the chamber: (a) annotated sensor locations before MLI placement and (b) the installed MLI configuration used to limit radiative exchange.

Metallic mating faces were inspected and cleaned with acetone followed by isopropyl alcohol. Grease was applied over the nominal 3 × 3 in area at the three internal SS304–SS304 interfaces. Braycote 601EF defines the calibration configuration and remains at the copper-to-stainless-steel and copper-to-copper fixture-edge films; Krytox LVP replaces only the internal coupon grease. The reduction uses applied bondline thicknesses of 128 µm for internal Braycote, 75 µm for fixture-edge Braycote, and 50.5 µm for internal Krytox.

Table 1. Layered-stack operating matrix used for calibration and transfer extraction

Case	Cold-side setpoint [°C]	Main-heater field [W]
A	75	20.1

Case	Cold-side setpoint [°C]	Main-heater field [W]
B	20	45.5
C	5	45.5
D	5	62.4

For each operating point, the cold plate was commanded to the Table 1 setpoint and the main heater used the listed field while the guard remained independently powered. Steady state was operationally recorded as RTD variation within ±1°C over at least 30 min, followed by a 15-min reported average. Case A is a bakeout/conditioning row with insufficient axial gradient for material-property extraction and is excluded from conductivity extraction and reported statistics; Cases B-D define each reported material/environment group.

THERMAL MODEL

The model is a steady-state lumped network with 17 temperature nodes representing the heater, guard, copper plates and sensor depths, stainless-steel sections, layered coupons, and cold-side region. Edges represent axial solid/TIM conduction, fixture and guard coupling, cold-plate coupling, radiation to the MLI environment, and effective ambient convection. It is a reduced one-dimensional model with lumped side paths, not a three-dimensional or transient solution. Each free node satisfies Equation (3).

Equation (3) defines steady-state energy conservation at free node i,

$$\sum_j G_{ij}\left(T_i - T_j\right) + \sum_b G_{ib}(T_i - T_b) = Q_i, \tag{3}$$

where j spans neighboring solved nodes, b spans prescribed measured boundaries, G_{ij} and G_{ib} are conductances in W/K, T denotes node temperature, and Q_i is applied nodal heat in W.

The remaining relations are stated individually below. Equations (4)–(8) define radiation, convection, and gap branches; Equations (9) and (10) define installed-joint and physical CMY resistance.

Equation (4) gives net radiative heat transfer,

$$Q_{\mathrm{rad}} = f_{\mathrm{r}}\, \varepsilon\, \sigma_{\mathrm{SB}}\, A\left({T_{\mathrm{s}}}^4 - {T_{\mathrm{sur}}}^4\right), \tag{4}$$

where Q_{rad} is radiative heat rate, f_r is the branch multiplier, ε is effective emissivity, σ_{SB} is the Stefan-Boltzmann constant, A is exchange area, and T_s and T_{sur} are absolute temperatures.

Equation (5) expresses the same radiative heat rate using an equivalent conductance,

$$Q_{\mathrm{rad}} = G_{\mathrm{rad}}(T_{\mathrm{s}} - T_{\mathrm{sur}}), \tag{5}$$

where G_{rad} is the radiative conductance in W/K, and $T_s - T_{sur}$ is the surface-to-surroundings temperature difference linearizing the radiative relationship.

Equation (6) defines the exact secant radiative conductance corresponding to Equation (4),

$$G_{\mathrm{rad}} = f_{\mathrm{r}}\, \varepsilon\, \sigma_{\mathrm{SB}}\, A\,(T_{\mathrm{s}} + T_{\mathrm{sur}})\left({T_{\mathrm{s}}}^2 + {T_{\mathrm{sur}}}^2\right), \tag{6}$$

where G_{rad} is radiative conductance in W/K, f_r is the branch multiplier, ε is effective emissivity, σ_{SB} is the Stefan-Boltzmann constant, A is exchange area, T_s is surface temperature, and T_{sur} is surroundings temperature; both temperatures are absolute.

Equation (7) gives effective ambient convective heat transfer,

$$Q_{\text{conv}} = h_{\text{eff}}\, A\, (T_{\text{s}} - T_{\text{air}}), \tag{7}$$

where Q_{conv} is convective heat rate, h_{eff} is the fitted heat-transfer coefficient, A is branch area, and T_s and T_{air} are surface and local-air temperatures.

Equation (8) gives stagnant-gap heat transfer,

$$Q_{\text{gap}} = \frac{Nu_{\text{gap}} k_{\text{air}}\, A}{g}\left(T_{\text{foil}} - T_{\text{guard}}\right), \tag{8}$$

where Q_{gap} is gap heat rate, Nu_{gap} is the gap Nusselt factor, k_{air} is air conductivity, A is gap area, g is gap thickness, and T_{foil} and T_{guard} are the bounding temperatures.

The radiative law uses a branch multiplier, effective emissivity, the Stefan-Boltzmann constant, and absolute temperature. Reported cases use diffuse-gray exchange with a unit radiation multiplier, effective emissivity 0.03 for stack/guard-to-MLI branches, and 0.80 for the heater to G10 branch. Ambient results use fitted effective top and side heat-transfer coefficients of 25.0 W/(m²·K), the upper bound, with TC4 as the local stack sink and TC5 as the top/guard sink.[12,13] The 6.35-mm foil gap uses a Nusselt factor of 1. Radiation is retained in both environments; convection and air-gap conduction are zeroed in vacuum.

The active chain includes heater-foil/block, copper-surface and RTD planes, either four monolithic-stainless positions or four layered-coupon centers, the lower copper planes, and the guard region. All boundary temperatures come from the retained case row. A passive-order check determines the extraction targets: consistent rows use RTD2 and RTD3 with RTD4 as the local cold anchor; an inconsistent row can impose RTD1/RTD4 as local boundaries, retain only the consistent internal target, and issue an applicability flag.

Calibration has two layers with different purposes. The physical layer assigns transferable fixture behavior before any Krytox extraction. Five selected temperatures from each of eight Braycote rows provide 40 temperature observations for ten fixture and installation terms: hot/cold fixture contacts, guard coupling, RTD3/RTD4 offsets, ambient side/top losses, hot/cold outer-fixture macro resistance, and internal Braycote installation resistance. Guard-energy, sensor-bias, and hot/cold contact-ratio residuals regularize that allocation but are not additional measurements. Bounded robust least squares, multiple starts, and residual-weighted refinement reduce dependence on initial values; fitted loss and macro terms remain model allocations rather than direct measurements.

After fixture calibration, all transferable parameters are frozen and a bounded scalar minimization searches 0.01–5.0 W/(m·K) for the conditional material-conductivity term. Termination tolerance is 1×10^{-7} W/(m·K) with at most 80 iterations. The objective is the summed squared residual over valid conductivity targets selected by the passive-order policy. Only Cases B-D enter casewise or group conductivity metrics; the Case A bakeout row remains excluded.

Comparator relations are evaluated only after extraction and do not enter calibration or fitting. Braycote agreement is calibration self-recovery. Krytox cross-material transfer is compared with the external Chemours relation through 0.119 W/(m·K) at 40 °C and 0.123 W/(m·K) at 100 °C.[14]

The standard identity, proprietary cell details, lot match, and comparator uncertainty were not supplied.

Internal SS304-SS304 joints use an overlap-corrected, grease-filled CMY model.[15,16] Total installed-joint resistance is the modeled bulk grease term, physical CMY resistance, and any separately fitted installation residual, as stated in Equation (9):

Equation (9) defines total installed-joint resistance,

$$R''_{\text{joint}} = \frac{L - Y}{k} + R''_{\text{CMY}} + R''_{\text{installation}}, \quad (9)$$

where R''_{joint} is total areal resistance, L is applied grease thickness, Y is mean-plane separation, k is conditional grease conductivity, R''_{CMY} is physical CMY resistance, and $R''_{installation}$ is the installation residual.

The physical CMY term is given by Equation (10):

Equation (10) defines physical CMY resistance as the inverse of parallel asperity and grease-gap conductance,

$$R''_{\text{CMY}} = \left[h_a + \frac{k}{Y}\right]^{-1}, \quad (10)$$

where R''_{CMY} is physical CMY resistance, h_a is asperity conductance, k is grease conductivity, and Y is mean-plane separation.

In the CMY calculation, asperity and grease-gap conductance act in parallel, and subtracting mean-plane separation from nominal film thickness avoids double counting the grease-filled roughness zone. The calculation uses 1.60 µm RMS roughness per SS304 face, 3.10–3.60 kPa nominal gravity preload, Gaussian surfaces, and complete grease filling and wetting. CMY resistance is model-derived and recalculated with grease conductivity; it is not a direct contact-resistance measurement.

RESULTS

Results proceed from the axial check to comparator agreement, installed response, and compact uncertainty, CMY, and residual diagnostics. Comparator differences are continuous diagnostics, and all Cases B-D are retained because no accuracy threshold was fixed prospectively. The monolithic SS304 coupon provided an axial heat-flow check by integrating the temperature-dependent SS304 conductivity between RTD2 and RTD3 and normalizing by listed main-heater power.[17]

Table 2 reports all 12 Cases B-D and the signed difference between grease conductivity and the comparator at the listed temperature. Braycote calibration self-recovery gives 2.20% casewise MAPE and 2.85% maximum absolute difference. Krytox cross-material transfer gives 2.28% MAPE and 5.10% maximum absolute difference. The agreement supports the transfer check but does not establish absolute measurement uncertainty.

Table 2. Full-calibration casewise grease-conductivity self-recovery and external-comparator validation for Cases B-D

Material	Env.	Case	Mean Temp. [°C]	k_{cond} [W/(m·K)]	k_{ref} [W/(m·K)]	Difference [%]
Braycote	Ambient	B	42.5	0.198	0.192	+2.8
		C	28.9	0.189	0.185	+2.1
		D	37.2	0.184	0.189	−2.8
	Vacuum	B	61.3	0.198	0.203	−2.0
		C	47.5	0.193	0.195	−1.2
		D	60.8	0.207	0.202	+2.1
Krytox	Ambient	B	40.0	0.123	0.119	+3.7
		C	26.8	0.116	0.118	−1.8
		D	34.4	0.113	0.119	−5.1
	Vacuum	B	58.0	0.123	0.120	+2.1
		C	46.0	0.119	0.119	−0.4
		D	58.7	0.119	0.120	−0.6

Table 2 reports casewise grease conductivity and the post-extraction comparator. Braycote agreement is calibration self-recovery, whereas Krytox tests cross-material transfer against the external relation. The configuration-specific installed response is retained because it does not require a unique conductivity/contact split. Braycote mean joint resistance is 6.624×10^{-4} m²·K/W in vacuum and 6.930×10^{-4} m²·K/W in ambient operation, with corresponding conductances of 1.511 and 1.444 kW/(m²·K). Krytox means are 4.196×10^{-4} and 4.310×10^{-4} m²·K/W, with conductances of 2.384 and 2.324 kW/(m²·K). At the tested internal heat fluxes of 4.86–10.42 kW/m², casewise joint resistance implies 2.33–6.66 K per modeled interface; three equivalent interfaces would contribute 6.99–19.97 K. That several-kelvin consequence makes installed-joint resistance the least ambiguous and most immediately useful thermal-network output.

Statistical analysis of repeated measurements was not conducted. The combined standard relative uncertainty spans 6.15–6.75%; the approximate expanded uncertainty at coverage factor 2 is 12.31–13.50%, dominated by the ±10% BLT input. The budget excludes comparator uncertainty, calibration covariance, repeatability/reassembly, drift, and distribution uncertainty and is not a traceable confidence interval or product-certification bound.[18]

A CMY ablation changed Krytox grease conductivity by no more than 0.0073%, indicating that the overlap-corrected CMY term primarily improves resistance bookkeeping at the tested preload. Krytox full-field residual RMS was 0.553 °C in ambient and 1.306 °C in vacuum.

CONCLUSIONS

TAIMV demonstrates the core functions of a modular ambient/vacuum interface testbed: interchangeable coupons, controlled boundaries, multiple through-stack sensors, an insulated chamber assembly, and operating points with resolvable axial gradients. Monolithic heat-rate ratios of 0.90–1.02 support axial consistency while remaining correctly separate from a whole-fixture calorimetric balance.

The 17-node balance and overlap-corrected contact resistance keep nominal grease thickness, a model-based intrinsic material-conductivity term, physical CMY contact, installation resistance, applied thermal conductivity, and total installed-joint resistance distinct. Krytox provides independent external-comparator validation of cross-material transfer: all six Cases B–D remain within 5.10% of the external relation without using that relation in calibration or extraction.

Expanded extraction uncertainty is 12.31–13.50%, with bond line thickness dominant. The evidence validates TAIMV as a full-matrix engineering testbed and installed-response extraction capability under the stated configuration. It is independent external-comparator validation, but not a blind or fully traceable intrinsic-property certification. This intended-use distinction is consistent with the evidence-based validation framework in ASME V&V 20.[19]

The next campaign should close the remaining metrology requirements with measured preload and in-load bond line thickness, at least three separate thicknesses, repeated disassembly/reassembly, traceable electrical and temperature calibration, mapped flatness/roughness, lot and application-mass records, and comparator uncertainty. Those additions are required before conductivity/contact separation or expanded uncertainty can be claimed as traceable material-property metrology.

The practical impact is a more defensible spacecraft thermal-input decision. Over the reported heat-flux domain, the installed-interface term represents 2.33–6.66 K per joint, large enough to change component margin and test or design decisions. TAIMV replaces substitution of a catalog bulk value with directly reported installed-joint resistance/conductance and applied conductivity, while retaining intrinsic material conductivity and contact resistance as explicitly model-conditioned outputs.

ACKNOWLEDGEMENTS

TAIMV was developed under an Amentum Innovation Grant at NASA Marshall Space Flight Center. Product names are used solely to identify the archived test configurations.

REFERENCES

1. NASA, 2026, "7.0 Thermal Control," State-of-the-Art of Small Spacecraft Technology, May 7, https://www.nasa.gov/smallsat-institute/sst-soa/thermal-control/ (accessed May 23, 2026).
2. Steinfeld, D., and Martins, M., 2019, "Interface Conductance Under a Real Electronics Box," NASA Report GSFC-E-DAA-TN70827, https://ntrs.nasa.gov/citations/20190030287.
3. Gregory, T., Abel, J., and Mandi, J., 2010, "Thermal Design Considerations of the Hubble Space Telescope (HST) Science Instrument Control and Data Handler (SI C&DH-2)," 40th International Conference on Environmental Systems, AIAA Paper 2010-6055, https://doi.org/10.2514/6.2010-6055; https://ntrs.nasa.gov/citations/20100025442.
4. Scialdone, J., Clatterbuck, C., and Wall, J., 1992, "Thermal Conductance of Two Interface Materials and Their Applications in Space Systems," 27th AIAA Thermophysics Conference, Nashville, TN, AIAA Paper 1992-2848, https://doi.org/10.2514/6.1992-2848; https://ntrs.nasa.gov/citations/19920010792.

5. Prasher, R., 2006, "Thermal Interface Materials: Historical Perspective, Status, and Future Directions," Proc. IEEE, 94(8), pp. 1571-1586, https://doi.org/10.1109/JPROC.2006.879796.
6. Due, J., and Robinson, A. J., 2013, "Reliability of Thermal Interface Materials: A Review," Appl. Therm. Eng., 50(1), pp. 455-463, https://doi.org/10.1016/j.applthermaleng.2012.06.013.
7. ASTM International, 2024, ASTM C1044-24, Standard Practice for Using a Guarded-Hot-Plate Apparatus or Thin-Heater Apparatus in the Single-Sided Mode, West Conshohocken, PA, https://doi.org/10.1520/C1044-24.
8. ASTM International, 2024, ASTM D5470-17(2024), Standard Test Method for Thermal Transmission Properties of Thermally Conductive Electrical Insulation Materials, West Conshohocken, PA, https://doi.org/10.1520/D5470-17R24.
9. Zhao, D., Qian, X., Gu, X., Jajja, S. A., and Yang, R., 2016, "Measurement Techniques for Thermal Conductivity and Interfacial Thermal Conductance of Bulk and Thin Film Materials," ASME J. Electron. Packag., 138(4), 040802, https://doi.org/10.1115/1.4034605.
10. Schacht, R., May, D., Wunderle, B., Wittler, O., Gollhardt, A., Michel, B., and Reichl, H., 2006, "Characterization of Thermal Interface Materials to Support Thermal Simulation," Proc. 12th International Workshop on Thermal Investigation of ICs and Systems (THERMINIC 2006), Nice, France, Sept. 27-29, ISBN 2-916187-04-9, https://arxiv.org/abs/0709.1849.
11. Kimmel, W. M., Beauchamp, P. M., Frerking, M. A., Kline, T. R., Vassigh, K. K., Willard, D. E., Johnson, M. A., and Trenkle, T. G., 2020, Technology Readiness Assessment Best Practices Guide, NASA/SP-20205003605, https://ntrs.nasa.gov/citations/20205003605.
12. Churchill, S., and Chu, H., 1975, "Correlating Equations for Laminar and Turbulent Free Convection From a Vertical Plate," Int. J. Heat Mass Transfer, 18(11), pp. 1323-1329, https://doi.org/10.1016/0017-9310(75)90243-4.
13. Churchill, S., 1977, "A Comprehensive Correlating Equation for Laminar, Assisting, Forced and Free Convection," AIChE J., 23(1), pp. 10-16, https://doi.org/10.1002/aic.690230103.
14. The Chemours Company, 2026, "Krytox LVP Thermal Conductivity and Specific-Heat Data," personal communication, Aug. 3. Conductivity values were derived by differential scanning calorimetry in a proprietary test cell against a standard of known thermal conductivity.
15. Yovanovich, M. M., 2005, "Four Decades of Research on Thermal Contact, Gap, and Joint Resistance in Microelectronics," IEEE Trans. Compon. Packag. Technol., 28(2), pp. 182-206, https://doi.org/10.1109/TCAPT.2005.848483.
16. Savija, I., Yovanovich, M. M., Culham, J. R., and Marotta, E. E., 2003, "Thermal Joint Resistance of Conforming Rough Surfaces with Grease-Filled Interstitial Gaps," J. Thermophys. Heat Transfer, 17(2), pp. 278-282, https://doi.org/10.2514/2.6763.
17. Touloukian, Y. S., 1966, Recommended Values of the Thermophysical Properties of Eight Alloys, Their Major Constituents and Oxides, NASA, https://ntrs.nasa.gov/citations/19660014513.
18. ASME, 2018, Test Uncertainty, ASME PTC 19.1-2018 (R2024), New York, NY, https://www.asme.org/codes-standards/find-codes-standards/test-uncertainty.

19. ASME, 2009, Verification and Validation in Computational Fluid Dynamics and Heat Transfer, ASME V&V 20-2009 (R2021), New York, NY, https://www.asme.org/codes-standards/find-codes-standards/standard-for-verification-and-validation-in-computational-fluid-dynamics-and-heat-transfer/2009.